Results in Physics 9 (2018) 628–635

Contents lists available at ScienceDirect

Results in Physics

journal homepage: www.journals.elsevier.com/results-in-physics

Strain and grain size of TiO_2 nanoparticles from TEM, Raman spectroscopy and XRD: The revisiting of the Williamson-Hall plot method

Pierre M. Kibasomba [a,b,c,d], Simon Dhlamini [c], Malik Maaza [a,d], Chuan-Pu Liu [e], Mohamed M. Rashad [f], Diaa A. Rayan [f], Bonex W. Mwakikunga [b,*]

[a] Department of Physics, Florida Research Centre, University of South Africa, Florida, South Africa
[b] DST/CSIR-National Centre for Nano-Structured Materials, PO Box 395 Pretoria, South Africa
[c] UNESCO-UNISA Africa Chair in Nanosciences/Nanotechnology, College of Graduate Studies, University of South Africa, Muckleneuk Ridge, P.O. Box 392, Pretoria, South Africa
[d] Nanosciences African Network (NANOAFNET), iThemba LABS-National Research Foundation, 1 Old Faure Road, Somerset West 7129, P.O. Box 722, Somerset West, Western Cape Province, South Africa
[e] Materials Science and Engineering, National Cheng Kung University, 1 University Rd, Tainan, Taiwan
[f] Centre for Metallurgical Research and Development Institute, (CMRDI), P.O. Box 87, Helwan, Cairo 11421, Egypt

ARTICLE INFO

Article history:
Received 9 December 2017
Received in revised form 1 March 2018
Accepted 3 March 2018
Available online 16 March 2018

Keywords:
Williamson-Hall
Scherrer
Particle
Crystallite
Strain
Size

ABSTRACT

The Williamson-Hall (W-H) equation, which has been used to obtain relative crystallite sizes and strains between samples since 1962, is revisited. A modified W-H equation is derived which takes into account the Scherrer equation, first published in 1918, (which traditionally gives more absolute crystallite size prediction) and strain prediction from Raman spectra. It is found that W-H crystallite sizes are on average 2.11 ± 0.01 times smaller than the sizes from Scherrer equation. Furthermore the strain from the W-H plots when compared to strain obtained from Raman spectral red-shifts yield factors whose values depend on the phases in the materials – whether anatase, rutile or brookite. Two main phases are identified in the annealing temperatures (350 °C–700 °C) chosen herein – anatase and brookite. A transition temperature of 550 °C has been found for nano-TiO_2 to irreversibly transform from brookite to anatase by plotting the Raman peak shifts against the annealing temperatures. The W-H underestimation on the strain in the brookite phase gives W-H/Raman factor of 3.10 ± 0.05 whereas for the anatase phase, one gets 2.46 ± 0.03. The new $\beta_{tot}^2\cos^2\theta$-$\sin\theta$ plot and when fitted with a polynomial yield less strain but much better matching with experimental TEM crystallite sizes and the agglomerates than both the traditional Williamson-Hall and the Scherrer methods. There is greater improvement in the model when linearized – that is the $\beta_{tot}\cos^2\theta$-$\sin\theta$ plot rather than the $\beta_{tot}^2\cos^2\theta$-$\sin\theta$ plot.

Introduction

Background

Comparing methods that determine particle size in nanocrystalline powders is ongoing as long as the problem of small particles remains unsolved [1]. A large chunk of research work points to the fact that the Williamson-Hall is more accurate, but over-estimate by ±35%, than the Scherrer method, worked out an improved Scherrer method on the basis of line width in the Scherrer equation and matched the calculation of W-H [2]. However, other research have shown that W-H underestimates by ±14% the particle size as compared to Scherrer, of which the correlation was confirmed with TEM [3].

The Williamson-Hall (W-H) method for crystallite size and strain analysis is still under-utilized as compared to the Scherer method, and yet it is more accurate and offers a greater benefit, the possibility of calculating, a very important material properties, in particular, structural parameter, the strain (ε), and phase composition. The W-H equation was derived in 1953 which was an improvement on the P. Scherrer (P-S) equation developed earlier before 1918 [4].

This W-H method is attributed to G.K. Williamson and his student, W.H. Hall [5]. It relies on the principle that the approximate formulae for size (Scherrer) broadening, β_L, and strain broadening, β_e, vary quite differently with respect to Bragg angle, θ:

* Corresponding author.
E-mail address: bmwakikunga@csir.co.za (B.W. Mwakikunga).

https://doi.org/10.1016/j.rinp.2018.03.008
2211-3797/

$$\beta_L = \frac{K\lambda}{L\cos\theta}; \beta_e = C\varepsilon\tan\theta \quad (1)$$

One contribution varies as 1/cosθ and the other as tanθ. If both contributions are present then their combined effect should be determined by convolution. The simplification of Williamson and Hall is to assume the convolution is either a simple sum or sum of squares. Using the former of these then one gets:

$$\beta_{tot} = \beta_L + \beta_e = C\varepsilon\tan\theta + \frac{K\lambda}{L\cos\theta} \quad (2)$$

If one multiplies this equation by cosθ one gets:

$$\beta_{tot}\cos\theta = C\varepsilon_{W-H}\sin\theta + \frac{K\lambda}{D_{W-H}} \quad (3)$$

where $D_{W\text{-}H}$ is the grain size as determined from the Williamson-Hall plot. Comparing this to the standard equation for a straight line (m = slope; c = intercept), y = mx + c, one sees that by plotting $\beta_{tot}\cos\theta$ versus $\sin\theta$ we obtain the strain component from the slope ($C\varepsilon$) and the size component from the intercept ($K\lambda/L$) or $K\lambda/D_{W\text{-}H}$. Such a plot is known as a Williamson-Hall plot. It can be a good idea to label each data point on the Williamson-Hall plot according to the index of its reflection to see whether any pattern emerges. It has been stated [6], however, that the Williamson-Hall method, owing to its many assumptions, should not be taken too seriously in terms of its absolute values but it can be a useful method if used in the relative sense; for example a study of many powder patterns of the same chemical compound, but synthesised under different conditions, might reveal trends in the crystallite size/strain which in turn can be related to the properties of the product.

It must be noted that there have been other proposals down through history on how to calculate the crystallite size from XRD data. One of them is the Halder-Wagner (HW) method given [7,8] by

$$\left(\frac{\beta_{tot}\cos\theta}{\sin\theta}\right)^2 = \frac{K\lambda}{D_{HW}}\cdot\frac{\beta_{tot}\cos\theta}{\sin^2\theta} + 16\varepsilon_{HW}^2 \quad (4)$$

where D_{HW} and ε_{HW} are Halder-Wagner crystallite size and strain respectively. Here, when a plot of $\left(\frac{\beta_{tot}\cos\theta}{\sin\theta}\right)^2$ is made against $\frac{\beta_{tot}\cos\theta}{\sin^2\theta}$ then a straight line graph of slope $\frac{K\lambda}{D_{HW}}$ and intercept $16\varepsilon_{HW}^2$ is obtained. Here, the slopes yield the Halder-Wagner crystallite size, D_{HW}, while the intercept gives the Halder-Wagner strain, ε_{HW}. However, the Halder-Wagner method is known be somewhat limited when compared to the Williamson-Hall method. When WH and HW methods were compared to some CeO_2 sample of pre-known average crystallite size 32 nm and strain 0.4(9)%, the WH method yielded the crystallite size of 29 nm whereas the HW method gave about 28 nm. Also, the WH yielded a strain of 0.4957% whereas the HW gave a strain value of 0.07682% [9–11]. Therefore it was reported that the HW method performed poorer than the WH method.

Current derivation of the new strain-crystallite-size equation

The intent of this paper is to report on the progress from post-Scherrer and post-W-H attempt to make the W-H equation accurate and more absolute than before. We do this by scaling the W-H crystallite size ($D_{W\text{-}H}$) against the more trusted Scherrer crystallite size (D_S). If we assume a linear proportionality between $D_{W\text{-}H}$ and D_S then we can write:

$$D_{W-H} = (D_{W-H})_0 + \alpha_{W-H-S}D_S = (D_{W-H})_0 + \alpha_{W-H-S}\frac{K\lambda}{\beta_{tot}\cos\theta} \quad (5)$$

Our second argument is that if the crystallite size by the W-H is not to be trusted as stated in Ref. [6], then it is difficult to conclude that the strain obtained from the same W-H method, $\varepsilon_{W\text{-}H}$ is accurate enough. This is the second reason for the need for a revision of the W-H method.

There are other more trusted methods for obtaining strain from crystallites. These include nano-indentation [12–13], red- or blue-shift of some phonons measured by either Raman spectroscopy [15–18] or FTIR [14–15] and high pressure anvil cell coupled to optical spectroscopic systems such as UV–Vis-IR spectrophotometer [16] and high pressure XRD and Raman spectroscopy [17–24]. As for Raman spectroscopy, the relationship between red- or blue-shift ($\Delta\omega$) of the phonon peaks and the tensile strain or compressive strain, ε_R, in the nano-crystals respectively is given by [14]

$$\omega = \omega_0\left(1 - \frac{a+r+3}{2}\varepsilon_R\right) \quad (6)$$

where a and r are constants to govern the attractive, a, and repulsive, r, exponents in the potential $V(l_b)$ of each bond; here, l_b is the length of the bond. [In order to shed more light on the potential $V(l_b)$ of the bond, the potential as a function of the bond length l_b is given as an additive sum of the repulsive component (A/l_b^r) and an attractive component $(-B/l_b^a)$ as $V(l_b) = (A/l_b^r)-(B/l_b^a)$]. The values of a and r are 6 and 12 for a van der Waal's bonding according to Leornad-Jones potential, 1 and 9 for ionic bonding and have a sum (a + r) of 3 for a covalent bonding [14]. The bonding in TiO_2 cannot be van der Waals nor ionic; therefore it is taken in this paper to be covalent and therefore we can express the relation between the new phonon frequency and the bulk frequency to

$$\omega = \omega_0\left(1 - \frac{3+3}{2}\varepsilon_R\right) = \omega_0(1 - 3\varepsilon_R) \quad (7)$$

Furthermore, if $\varepsilon_{W\text{-}H}$ and ε_R scale linearly with each other, then one can write:

$$\varepsilon_{W-H} = (\varepsilon_{W-H})_0 \pm \gamma\varepsilon_R \quad (8)$$

Since the traditional Williamson-Hall strain, $\varepsilon_{W\text{-}H}$, is an underestimated value, one then chooses the + rather than the – in Eq. (8). Therefore the new strain, ε', is

$$\varepsilon' = (\varepsilon_{W-H})_0 + \gamma\varepsilon_R \quad (9)$$

Then one can derive a new equation from the Williamson-Hall by substituting Eqs. (4)-(7) into Eq. (3) as follows:

$$\beta_{tot}\cos\theta = C\varepsilon'\sin\theta + \frac{K\lambda}{(D_{W-H})_0 + \alpha_{W-H-S}\frac{K\lambda}{\beta_{tot}\cos\theta}} \quad (10)$$

This means that a plot of $\beta_{tot}\cos\theta$ versus $\sin\theta$ will not give a linear plot assumed by Williamson and Hall in 1962. Indeed further analysis of Eq. (10) yields:

$$\begin{aligned}
&\beta_{tot}\cos\theta\left[(D_{W-H})_0 + \alpha_{W-H-S}\frac{K\lambda}{\beta_{tot}\cos\theta}\right] \\
&= C\varepsilon'\sin\theta\left[(D_{W-H})_0 + \alpha_{W-H-S}\frac{K\lambda}{\beta_{tot}\cos\theta}\right] \\
&\quad + K\lambda(D_{W-H})_0\beta_{tot}\cos\theta + \alpha_{W-H-S}K\lambda \\
&= (D_{W-H})_0 C\varepsilon'\sin\theta + \\
&\Rightarrow C\varepsilon'\sin\theta\alpha_{W-H-S}\frac{K\lambda}{\beta_{tot}\cos\theta}\left[(D_{W-H})_0 + \alpha_{W-H-S}\frac{K\lambda}{\beta_{tot}\cos\theta}\right] + K\lambda \\
&\Rightarrow \beta_{tot}\cos\theta(D_{W-H})_0 + \alpha_{W-H-S}\frac{K\lambda}{\beta_{tot}\cos\theta} \\
&= C\varepsilon'\sin\theta\left[(D_{W-H})_0 + \alpha_{W-H-S}\frac{K\lambda}{\beta_{tot}\cos\theta}\right] + K\lambda
\end{aligned} \quad (11)$$

or

$$\beta_{tot}^2\cos^2\theta(D_{W-H})_0 + \alpha_{W-H-S}K\lambda = C\varepsilon'\beta_{tot}\cos\theta\sin\theta\left[(D_{W-H})_0 + \alpha_{W-H-S}\frac{K\lambda}{\beta_{tot}\cos\theta}\right] + K\lambda\beta_{tot}\cos\theta \quad (11a)$$

$$\Rightarrow (D_{W-H})_0\beta_{tot}\cos\theta + \alpha_{W-H-S}K\lambda = (D_{W-H})_0C\varepsilon'\sin\theta + C\varepsilon'\alpha_{W-H-S}\frac{K\lambda\sin\theta}{\beta_{tot}\cos\theta} + K\lambda$$
$$\Rightarrow (D_{W-H})_0\beta_{tot}^2\cos^2\theta + \alpha_{W-H-S}K\lambda\beta_{tot}\cos\theta = (D_{W-H})_0C\varepsilon'\beta_{tot}\cos\theta\sin\theta + C\varepsilon'\alpha_{W-H-S}K\lambda\sin\theta + K\lambda\beta_{tot}\cos\theta$$
$$\Rightarrow (D_{W-H})_0\beta_{tot}^2\cos^2\theta + (\alpha_{W-H-S}-1)K\lambda\beta_{tot}\cos\theta = (D_{W-H})_0C\varepsilon'\beta_{tot}\cos\theta\sin\theta + C\varepsilon'\alpha_{W-H-S}K\lambda\sin\theta$$
$$\Rightarrow (D_{W-H})_0\beta_{tot}^2\cos^2\theta = (D_{W-H})_0C\varepsilon'\beta_{tot}\cos\theta\sin\theta + C\varepsilon'\alpha_{W-H-S}K\lambda\sin\theta - (\alpha_{W-H-S}-1)K\lambda\beta_{tot}\cos\theta \quad (11b)$$

If one uses the trigonometric identities of $\cos^2\theta + \sin^2\theta = 1$, one gets

$$(D_{W-H})_0\beta_{tot}^2\cos^2\theta = (D_{W-H})_0C\varepsilon'\beta_{tot}(1-\sin^2\theta)^{\frac{1}{2}}\sin\theta + C\varepsilon'\alpha_{W-H-S}K\lambda\sin\theta - (\alpha_{W-H-S}-1)K\lambda\beta_{tot}(1-\sin^2\theta)^{\frac{1}{2}} \quad (12)$$

And after expanding the binomial series and neglecting the higher terms, one gets

$$(D_{W-H})_0\beta_{tot}^2\cos^2\theta = (D_{W-H})_0C\varepsilon'\beta_{tot}\left(1-\frac{1}{2}\sin^2\theta\right)\sin\theta + C\varepsilon'\alpha_{W-H-S}K\lambda\sin\theta - (\alpha_{W-H-S}-1)K\lambda\beta_{tot}\left(1-\frac{1}{2}\sin^2\theta\right) \quad (13)$$

And further simplification and re-arrangement yields

$$(D_{W-H})_0\beta_{tot}^2\cos^2\theta = -(D_{W-H})_0C\varepsilon'\beta_{tot}\frac{1}{2}\sin^3\theta + \frac{1}{2}(\alpha_{W-H-S}-1)K\lambda\beta_{tot}\sin^2\theta + [(D_{W-H})_0C\varepsilon'\beta_{tot} + C\varepsilon'\alpha_{W-H-S}K\lambda]\sin\theta - (\alpha_{W-H-S}-1)K\lambda\beta_{tot} \quad (14a)$$

$$\beta_{tot}^2\cos^2\theta = a\sin^3\theta + b\sin^2\theta + c\sin\theta + d \quad (14b)$$

The implication of this equation is that a plot of $\beta_{tot}^2\cos^2\theta$ versus $\beta_{tot}\sin\theta$ is a non-linear curve which describes a cubic polynomialy = $ax^3 + bx^2 + cx + d$ where

$$a = \frac{-\frac{1}{2}(D_{W-H})_0C\varepsilon'}{(D_{W-H})_0};\quad b = \frac{\frac{1}{2}(\alpha_{W-H-S}-1)K\lambda}{(D_{W-H})_0};$$
$$c = \frac{[(D_{W-H})_0C\varepsilon' + C\varepsilon'\alpha_{W-H-S}K\lambda]/\beta_{tot}}{(D_{W-H})_0};\quad d = \frac{-(\alpha_{W-H-S}-1)K\lambda}{(D_{W-H})_0}$$

or

$$a = -\frac{1}{2}C\varepsilon';\quad b = \frac{\frac{1}{2}(\alpha_{W-H-S}-1)K\lambda}{(D_{W-H})_0};\quad c = C\varepsilon' + \frac{C\varepsilon'\alpha_{W-H-S}K\lambda}{\beta_{tot}(D_{W-H})_0};$$
$$d = \frac{-(\alpha_{W-H-S}-1)K\lambda}{(D_{W-H})_0}$$

This means that the new strain, ε', is found from the coefficient of the $\sin^3\theta$ and the new particle size from intercept as well as from the coefficient of $\sin^2\theta$.

Therefore, the new strain is found from the intercept of the cubic polynomial as follows:-

$$\varepsilon' = \frac{-2a}{C} = -\frac{1}{2}a \quad (15)$$

And the Williamson-Hall to Scherrer parameter, α_{W-H-S}, and the threshold particle size, $(D_{W-H})_0$ are found by solving the equations for b and d simultaneously and the simplification lead to:

$$\alpha_{W-H-S} = \frac{2b}{d+2b} + \frac{1}{K\lambda} \quad (16)$$

and

$$(D_{W-H})_0 = \frac{K\lambda}{d+2b} \quad (17)$$

The main task in this theory is to transform the β_{tot}-θ data into a plot of $\beta_{tot}^2\cos^2\theta$ against $\sin\theta$ rather than the traditional $\beta_{tot}\cos\theta$ against $\sin\theta$ plot and fit Eq. (14) to this plot and extract coefficients a, b, c, and d. Coefficient a is used to find the strain in the sample and coefficients b and d contain information on particle size.

The second option is to linearize Eq. (14). This is accomplished by neglecting the higher powers of $\sin\theta$ and then reducing Eq. (14) to

$$\beta_{tot}\cos^2\theta \cong C\varepsilon'\left[1+\frac{\alpha_{W-H-S}K\lambda}{\beta_{tot}(D_{W-H})_0}\right]\sin\theta - \frac{(\alpha_{W-H-S}-1)K\lambda}{(D_{W-H})_0} \quad (18)$$

where the slope is equal to $C\varepsilon'\left[1+\frac{\alpha_{W-H-S}K\lambda}{\beta_{tot}(D_{W-H})_0}\right]$. This means that the new strain ε' is further increased by a factor of $\frac{\alpha_{W-H-S}K\lambda}{\beta_{tot}(D_{W-H})_0}$. Also the intercept which is equal to $\frac{(\alpha_{W-H-S}-1)K\lambda}{(D_{W-H})_0}$ is used to calculate the crystallite size. We will leave to the reader to find out that the strain comes close to the much trusted Raman strain and, similarly, the particle or crystallite size comes down to the values of crystallites sizes obtained from TEM imaging.

Experimental details

Two samples were used in the experiment: the first sample, Ti-iso-2-450, the lyophilized sample. We refer to it as temperature programmed synthesis TiO_2 from isopropoxide precursor at fixed pH value. The second, P-25 Degussa, the commercial TiO_2, mainly composed of anatase (99.2%).

The TiO_2 nanoparticles were synthesized by a multi-step, adapted version of the lyophilization technique. 1.0 g of titanium isopropoxide was dissolved in 150 ml of distilled water and brought to a pH of 7. The solution was sprayed "laminar regime" into liquid nitrogen in order to generate droplets rich in water (~90%). These droplets were then sublimated in a lyophiliser chamber to yield a very porous precursor. The precursor was then thermally decomposed at 450 °C in air for about 1 h to form TiO_2 nanoparticles.

For the study of the particle size and strain evolution of TiO_2, a set of samples of nanoparticles with discrete sizes was required. Samples Ti-iso-2-450, Ti-iso-550, Ti-iso-2-650, Ti-iso-2-700 and Ti-iso-900 were prepared by starting heating the amorphous titania in air for 1 h at 350 °C, 400°, 450 °C, 550 °C, 650 °C and 700 °C respectively.

The X-ray diffraction patterns of the film were measured at room temperature using the Panalytical XPERT PRO PW3050/50 diffractometer with CuKα radiation (45 kV, 400 mA, λ = 0.1540598 nm and $5° \le 2\theta \le 90°$). And the spectra were analysed with reference to Refs. [21–32]. The Auriga ZEISS Scanning electron microscope (SEM) was employed to study the morphology of the film and to estimate the thickness of oxide layers that are present.

Raman spectroscopy was carried out using a Jobin–Yvon T64000 Raman spectrograph with a 514.5 nm line from an argon ion laser. The power of the laser at the sample at the post-annealed samples was small enough (0.384 mW) in order to minimise localised heating of the sample. The T64000 was operated in single spectrograph mode, with the 1800 lines/mm grating and three objective lenses on the microscope with the following magnifications: 20×, 50× and 100×. Strain values for each samples were obtained by employing Eq. (6).

The samples were further characterized using high resolution TEM (HRTEM, JOEL-JEM 2100).

Results and discussion

Transmission electron microscopy (TEM) revealed 10–20 nm rounded and also faceted anatase nano-crystallites, Fig. 1. TEM studies of the sample Ti-iso-700 indicated an oriented-aggregation crystal growth pathways (Fig. 1).

Along this pathway, whereby small crystals grow differently from larger crystals, the small crystals aggregate in such a way that the adjacent surfaces share the same crystallographic orientation. In the process, the pair of adjacent interfaces are eliminated and the pair of nanoparticles are converted to a larger single-crystal. Due to this aggregation, the final particle size may reach large particle size up to 80 nm. Energy dispersive X-ray (EDS) measurements (not shown) conducted on these nanoparticles confirmed the TiO_2 stoichiometric composition of lyophilized anatase (sample Ti-*iso*-2-700) or comparison, a TEM micrograph of Degussa P25 is given in Fig. 1(b). Both spherical and faceted considerably larger particles, typically varying in size from 50 to 250 nm, have been seen compared to the sample made by the lyophilization technique.

The X-ray diffraction analysis was completed on the lyophilized samples Ti-iso-2 nanopowders, using the diffractometer with a Cu-Kα target (wavelength λ = 0.15409 nm). The experiment was ran from angle of 10° to angle of 70°, at 0.0333° step.

Fig. 2(a) summarizes the results from XRD analysis of the five annealed samples – 350, 450, 550, 650 and 700 °C. It can be observed that the (1 0 1) direction is the most preferred orientation and this direction is enhanced as the annealing temperature is raised. There are more crystallite planes which are maintained regardless of annealing temperature which indicates the polycrystallinity of the samples as well as the fact that there more than one phase in the materials.

Raman spectra of the same samples given in Fig. 2(b) reveal the preferred phonon of 150 cm^{-1} which is an indication of anatase phase. The phonon frequency (wavenumber) position is however observed to change and shift to lower wavenumbers as demonstrated by a dotted line in Fig. 2(b) showing that the annealing causes a strain in the crystallites. Since redshift is confirmed suggests that the strain is tensile in accordance with Eq. (5) in the previous sections.

Particle size and strain calculation

The average crystallite size was estimated using Scherer size and compared to the one found using Williamson-Hall method, and the strain was only estimated from the W-H method (plotting $\beta_{tot}\cos\theta$ against $\sin\theta$) as well as the Raman strain values obtained from Fig. 2 (b) via Eq. (6). For some of the samples, by plotting $\beta_{tot}\cos\theta$ against $\sin\theta$, we obtain a linear profile. Observing dots spread across the linear plot of $B_s\cos\theta$ versus $\sin\theta$, the distribution is typical detail displayed by substance that accounts for elastic deformation due to thermal stress, thus an average linear profile traced through the entire range requires a characteristic data validation. For some plots that are non-linear, one often ascribes this to multiple phases in the sample. However, the reader will see that this calls for a revision of the W-H plot to take into account these non-linearities as will be discussed in the upcoming sections.

The analysis of the XRD diffractograms by the Williamson-Hall (W-H) plot ($\Gamma\cos\theta = K\lambda/D + 4\varepsilon\sin\theta$) [29] and the Debye-Scherrer (D-S) equation (($\Gamma\cos\theta = K\lambda/D$) [30–46] have been achieved extensively before. Here, Γ is the full-width-at-half-maximum (FWHM) of the ith peak, θ is the angle at which the ith peak is found in radians, K is a constant for a given instrument alignment which usually about 0.9, λ is the wavelength of the X-rays employed which for this case the X-ray are from Cu K_α at 1.54 Å, D_S is the Scherrer crystallite size and ε is the strain.

Fig. 3 summarizes the analyses for crystallite sizes and strain calculations from XRD and Raman spectra of the five annealed samples. In Fig. 3(a) are summarized the phonon frequency shift of the 150 cm-1, crystallite size by Scherrer and W-H methods and strains from W-H method and Raman spectra. The phonon red-shift is evidence of tensile stress. The plot demonstrates a slight increase in the phonon wavenumber after 550 °C before it continues to decrease after 600 °C. Blue shifts at an annealing temperature of 550 °C suggest a change of phase which is a non-reversible transformation from anatase to brookite [30,32,33].

The phase changes signalled by phonon position and broadenings are more evident in the amplified Fig. 3(b) where these transition temperatures can be 570 °C when phonon peak positions are used but one can identify three phases with transition temperatures 450 [from anatase to brookite] and 650 °C [from

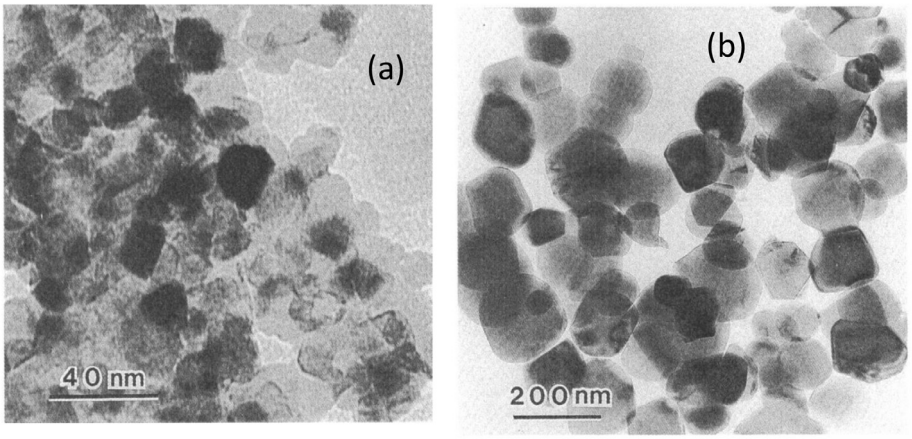

Fig. 1. (a) Lyophilized TiO_2 nanoparticles and annealed at 700 °C (b) Degussa P25 TiO_2 nanoparticles.

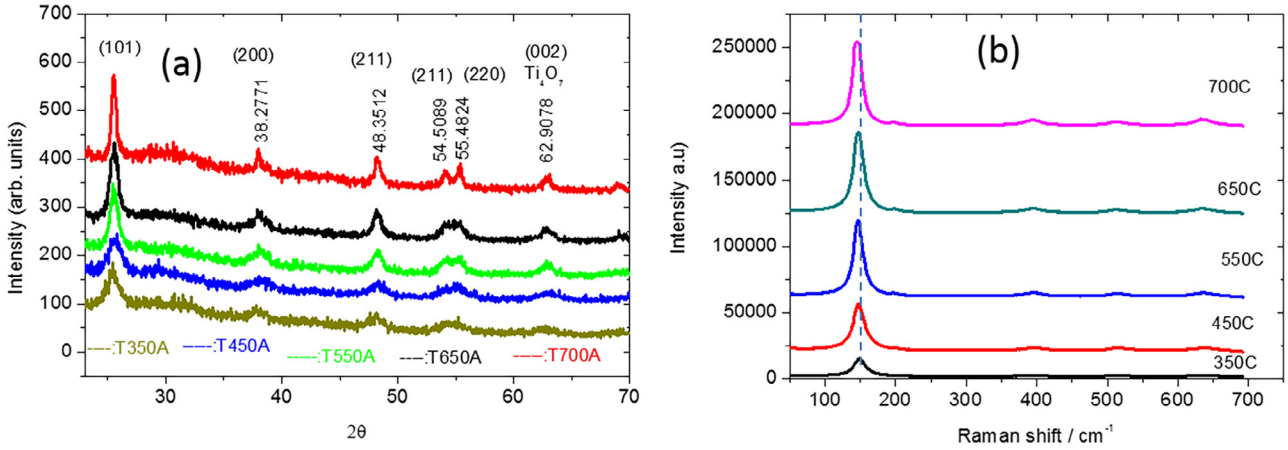

Fig. 2. (a) XRD diffractograms and (b) Raman spectra of the all lyophilized TiO_2 annealed at 350, 450, 550, 650 and 700 °C.

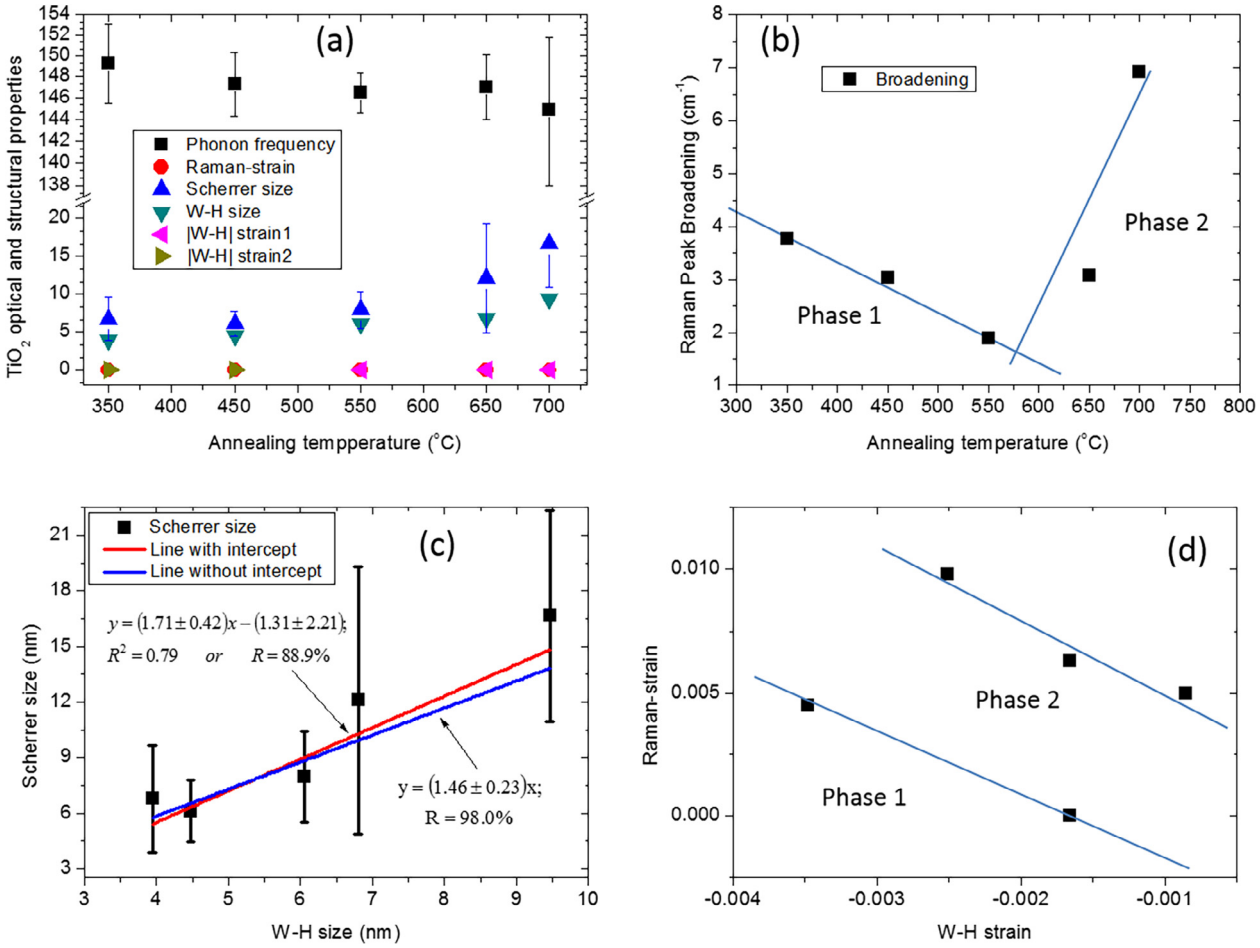

Fig. 3. (a) Williamson-Hall crystallite size (b) W-H strain/broadening versus annealing temperature with broadening-temperature plot revealing a transition temperature of 570 °C (c) Williamson-Hall crystallite size vs Scherrer crystallite size showing that Williamson-Hall plot underestimates crystallite size by 50% (d) Williamson-Hall strain vs Raman strain underestimates strain depending on whether it composite of all phases, or phase 1 only or phase 2 only by 170%, 31% and 25% respectively.

brookite to rutile] when strains calculated from W-H method as well as Raman spectra as shown by the dotted lines in Fig. 3(b). One also notes that again the strain values obtained from the W-H method are consistently less than those obtained from Raman spectral method.

The crystallite size by both methods increases with annealing temperature. However, the W-H method yields crystallite sizes consistently smaller than those obtained from the Scherrer method.

The observation that the traditional W-H method underestimates both the crystallite size and the strain value forced us to investigate the magnitude of these under-estimations. In Fig. 3 (c) we show a plot of Scherrer size, D_S, against the W-H size, $D_{W\text{-}H}$, which gives $D_S = (1.71 \pm 0.42)D_{W-H} - (1.31 \pm 2.21)$ when

intercept is considered. However, when the intercept is not considered then $D_S = (1.46 \pm 0.23)D_{W=H}$.

In Fig. 4(a) the Williamson-Hall plot shows that the TiO_2 sample annealed at 350 °C reveals non-linearity. This demonstrates that at such low temperatures, the TiO_2 has more than one phase in it as both positive and negative strains apparent from the plot which suggests non-homogeneity in the particles size as many intercepts on the y-axis are possible. At 450 °C the evidence of two distinct linear graphs emerge with two different strains. The two lines tend to point to one y-intercept which means homogeneity in particle. At 550 and 650 °C, the plot shows that the samples return to the 350 °C situation, only that there are two phases – one with positive strain and the other bearing a negative strain – are now more distinct. At 700 °C the two phases continue to exist conserving the crystallite sizes albeit with different strains.

As seen in Fig. 4(b) the modified W-H- method (plotting $\beta^2_{tot}\cos^2\theta$ against $\sin\theta$) was employed in the calculation of both new strain values and new particles sizes for the five samples annealed at different temperatures. This is accomplished by fitting the presently derived Eq. (14) or its shorthand in Eq. (15) and extracting the coefficients, a, b, c, and d in the cubic polynomial. Eqs. (15)–(17) are then employed in the calculation of the new strain, ε', the Williamson-Hall-to-Scherrer particles size parameter, $\alpha_{W\text{-}H\text{-}S}$, the threshold particle size $(D_{W\text{-}H})0$ and hence the new particles size $D'_{W\text{-}H}$. Table 1 summarized all data discussed in this paper for the samples annealed at 350, 450, 550, 650, and 700 °C. One observes from the table, as also given in Fig. 3(a) that the W-H method gives the least particles sizes (from 1 nm to about 3 nm). This is followed by the Scherrer method which also slight underestimates the particle size and does not take into account any agglomerations. Although the new $\beta^2_{tot}\cos^2\theta$ - $\sin\theta$ method yields very small strains when compared to the more trusted Raman spectroscopy method, new method's threshold particles is much more closer to the particle sizes found from high resolution TEM than both the Williamson-Hall and the Scherrer sizes When the Scherrer factor is added to this threshold value, the new method then also accounts for agglomerates.

Further to the $(\beta_{tot}\cos\theta)^2$-$\sin\theta$ method discussed so far, it was important, in this study, to try the linear version of Eq. (14) i.e. the $\beta_{tot}\cos^2\theta$-$\sin\theta$ plot as suggested in Eq. (16). When a plot of $\beta_{tot}\cos^2\theta$ was made against $\sin\theta$, shown Fig. 4(c), and linear equations fitted to the data, the slopes and intercepts from this plot helped calculate the strains and crystallite sizes for the samples respectively. The data from such a fit are summarized in Table 2. The strains are in the order of 10-3 which one order of magnitude higher that in the cubic model or the $(\beta_{tot}\cos\theta)^2$-$\sin\theta$ method. The crystallite sizes are much higher than both the Scherrer and

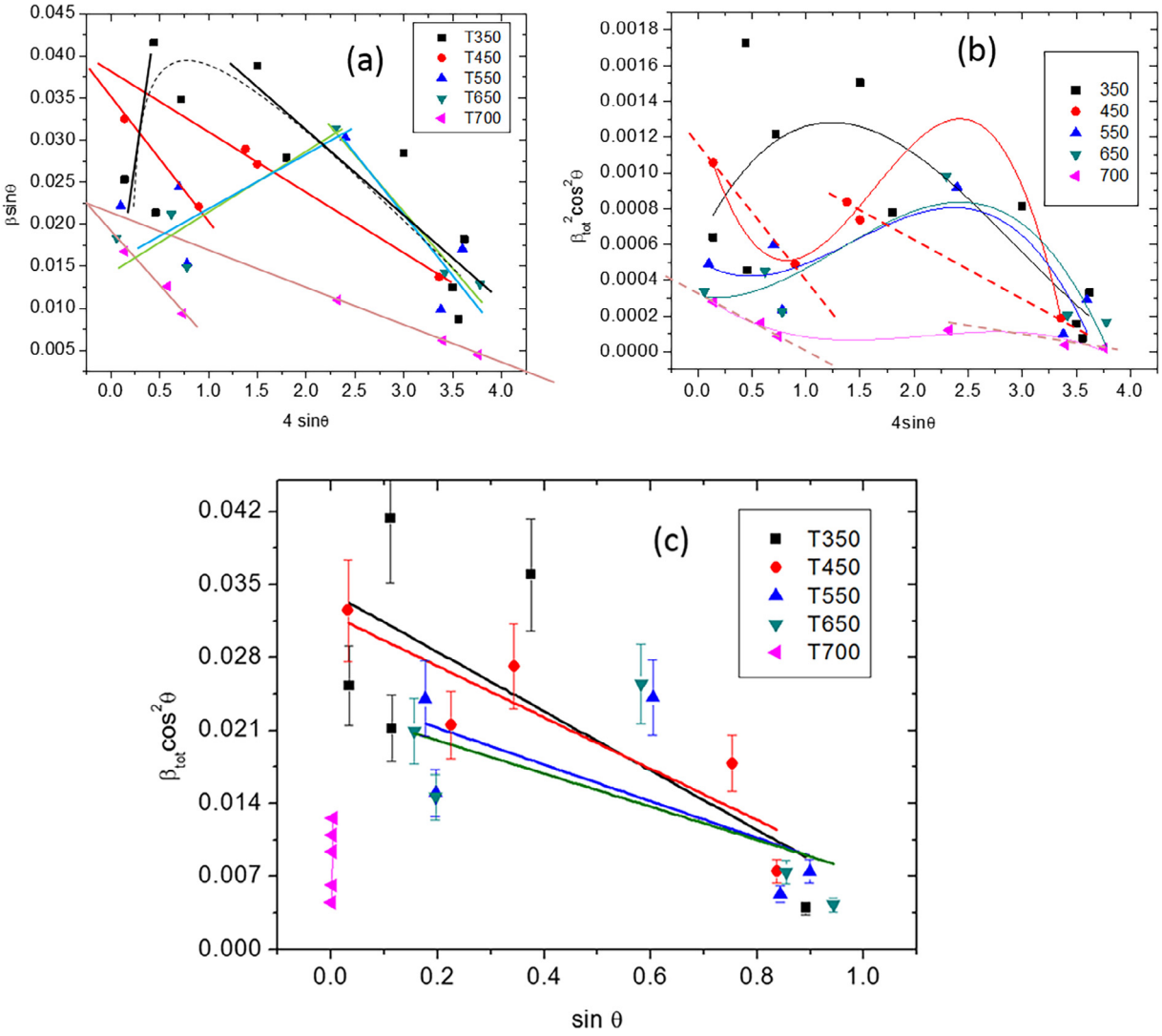

Fig. 4. (a) A Williamson-Hall plot of $\beta_{tot}\cos\theta$ against $C\sin\theta$ (where C = 4) calculated from XRD spectra for lyophilized TiO_2 samples annealed at 350, 450, 550, 650 and 700 °C.

Table 1
Summary of all data calculated from XRD data by Scherrer method (particle size D_S), the Williamson-Hall method (the particle size $D_{W\text{-}H}$ and strain $\varepsilon_{W\text{-}H}$) the modified Williamson-Hall (the new threshold particles size $(D_{W\text{-}H})_0$ and the new particles size $D'_{W\text{-}H}$) and Raman spectroscopy analysis for strain ε_{Raman}.

Annealing T (°C)	D_S (nm)	$D_{W\text{-}H}$ (nm)	$\varepsilon_{W\text{-}H}$	ε_{Raman}	a	ε'	b	d	R^2	$(D_{WH})_0$	D′
350	4.62 ± 1.06	2.2944	0.0493	0.153323	4.17E−04	2.09E−04	0.0075	0.00667	−0.66265	71.10752	80.85572
450	7.32 ± 5.14	2.5124	0.5907	1.837077	0.00126	6.30E−04	−0.00755	−0.02073	0.82836	43.0059	27.5607
550	5.25 ± 0.78	0.4479	0.41	1.2751	−0.00139	−6.95E−04	0.01375	0.01111	−0.51696	39.90935	50.98685
650	9.37 ± 1.28	2.6445	0.1914	0.595254	−5.68E−04	−2.84E−04	0.0067	0.00236	0.03677	97.77284	117.5435

Table 2
Summary of parameters extracted from the linearized demonstrating that a plot of $\beta_{tot}\cos^2\theta$-$\sin\theta$ method yields the new strain which are increased by a significant factor – about one order of magnitude higher than both the W-H and H-W method and the present $\beta^2_{tot}\cos^2\theta$-$\sin\theta$ method. This comes close to the desired accuracy as in the strains obtained by Raman spectroscopy. This also forced the crystallite size to approach the values obtained by HRTEM imaging.

Anneal T (°C)	D_S	Intercept	Slope	Mean grain size from TEM (nm)	ε	D_0 (nm)	D′ (nm)
350	4.62	$34.22 \pm 7.56 \times 10^{-3}$	$-(28.43 \pm 1.72) \times 10^{-2}$	15	−0.00711	4.5	14.2
450	7.32	$32.1 \pm 3.83 \times 10^{-3}$	$-(24.61 \pm 0.72) \times 10^{-2}$	20	−0.00615	4.8	20.2
550	5.25	$24.77 \pm 6.82 \times 10^{-3}$	$-(1.757 \pm 1.09) \times 10^{-3}$	25	−0.00439	6.2	17.3
650	9.37	$23.22 \pm 6.84 \times 10^{-3}$	$-(1.588 \pm 1.08) \times 10^{-3}$	28	−0.00397	6.6	26.4

Williamson-Hall sizes and are in perfect agreement the HRTEM measured crystallite sizes.

Conclusion

We have introduced a revision of the Williamson-Hall equation. This was necessitated by the gross underestimation of the crystallite sizes worse than the Scherrer formula. When compared to TEM crystallite sizes, we found that Scherrer sizes are also slightly less, withn experimental error, than the TEM sizes. The revision was accomplished through the expansion of the W-H equation into a full polynomial equation which after further binomial expansion via some trigonometric identities reduced to a cubic polynomial. The main task in this theory is to transform the β_{tot}-θ data into a plot of $\beta^2_{tot}\cos^2\theta$ against $\sin\theta$ rather than the traditional $\beta_{tot}\cos\theta$ against $\sin\theta$ plot and fit Eq. (14) to this plot and extract coefficients a, b, c, and d. Coefficient a is use to find the strain in the sample and coefficients b and d contain information on particle size. Although the our $\beta^2_{tot}\cos^2\theta$-$\sin\theta$ method yields strain values are surprisingly very small when compared to the more trusted Raman spectroscopy method, new method's threshold particles is much more closer to the particle sizes found from high resolution TEM than both the Williamson-Hall and the Scherrer sizes When the Scherrer factor is added to this threshold value, the new method then also accounts for agglomerates as the particles size in the current results set range in hundreds of nanometers. It has been shown that when the current model is linearized – $\beta_{tot}\cos^2\theta$-$\sin\theta$ method- the new strain is increased by a significant factor – about one order of magnitude higher than the $\beta^2_{tot}\cos^2\theta$-$\sin\theta$ method and coming close to the desired accuracy as in the strains obtained by Raman spectroscopy. This also forced the crystallite size to approach the values obtained by TEM imaging.

Acknowledgements

The sponsorships of the South Africa-Taiwan Bilateral Programme (HGER31X) and the South Africa- Egypt Bilateral Programme (HGER40X) through the National Research Foundation (NRF) in Pretoria, South Africa are highly acknowledged.

References

[1] Gonçalves NS, Carvalho JA, Lima ZM, Sasaki JM. Size-strain study of NiO nanoparticles by X-ray powder diffraction line. Mater Lett 2012;72:36–8.
[2] Khorsand Zak A, Abd Majid WH, Abrisham ME, Yousfi Ramin. X-ray of ZnO nanoparticles by Williamson-Hall and size-strain plot methods. Solid State Sci 2011;13:251–6.
[3] Mote VD, Purushotham Y, Dole BN. Williamson-Hall analysis in estimation of lattice strain in nanometer-sized ZnO particles. J Theor Appl Phys 2012;6:6.
[4] Scherrer P. Bestimmung der Grösse und der inneren Struktur von Kolloidteilchen mittels Röntgenstrahlen. Nachr Ges Wiss Göttingen 1918;26:98–100.
[5] Williamson GK, Hall WH. X-ray line broadening from filed aluminium and wolfram. Acta Metall 1953;1:22–31.
[6] http://pd.chem.ucl.ac.uk/pdnn/peaks/sizedet.htm.
[7] Halder NC, Wagner CNJ. Separation of particle size and lattice strain in integral breadth measurements. Acta Crystallogr 1966;20:312–3.
[8] Halder NC, Wagner CNJ. analysis of the broadening of powder pattern peaks using variance, integral breadth, and fourier coefficients of the line profile. Adv X-Ray Anal 1966;9:91–102.
[9] Ida T, Shimazaki S, Hibino H, Toraya H. Diffraction peak profiles from spherical crystallites with lognormal size distribution. J Appl Cryst 2003;36:1107–15.
[10] Izumi F, Ikeda T. Implementation of the Williamson-Hall and Halder-Wagner methods in the RIETAN-FP. Adv Inst Sci Technol 2014;3:33–8.
[11] Chen KW, Jian SR, Wei PJ, Jang JSC, Lin JF. A study of the relationship between semi-circular shear bands and pop-ins induced by indentation in bulk metallic glasses. Intermetallics 2010;18:1572–7.
[12] Kumar A, Yedla N. Mechanical and structure studies of $Zr_{50}Cu_{50}$ glass matrix composites during nano-indentation-a molecular dynamics study. IOP Conf Ser: Mater Sci Eng 2015;75:012020.
[13] Kim J-J, Choi Y, Suresh S, Argon AS. Nanocrystallization during nanoindentation of a bulk amorphous metal alloy at room temperature. Science 2002;295:654–7.
[14] Gouadec G, Colomban P. Raman spectroscopy of nanomaterials: how spectra relate to disorder. Particle Size and Mechanical Properties. The open archive HAL.
[15] Beams R, Cancado LG, Novotny L. Raman characterization of defects and dopants in graphene. J Phys: Condens Matter 2015;27:083002.
[16] Ferrari AC, Basko DM. Raman spectroscopy as a versatile tool for studying the properties of graphene, Mat. Science (condensed-materials). Nat Nanotechnol 2013;8:235.
[17] Kumar S, Tiwari N, Jha SN, Chatterjee S, Bhattacharyya D, Ghosh AK. Structural and optical properties of sol–gel derived Cr-doped ZnO diluted magnetic semiconductor nanocrystals: an EXAFS study to relate the local structure. RSC Adv 2016;Issue 109, Issue in Progress doi.org/10.1039/c6ra15685a.
[18] Bera D, Qian L, Tseng T-K, Holloway PH. Quantum dots and their multimodal applications: a review. Materials 2010;3:2260–345. https://doi.org/10.3390/ma3042260.
[19] Stella C, Soundararajan N, Ramachandran K. Structural, optical, and magnetic properties of Mn and Fe-doped Co_3O_4 nanoparticles. AIP Adv 2015;5:087104.
[20] Guerbous L, Boukerika A. Nanomaterial host bands effect on the photoluminescence properties of Ce-Doped YAG Nanophosphor synthesized by Sol-Gel method. J Nanomater 2015;2015:617130–40.
[21] Dhara S, Giri PK. Size-dependent visible absorption and fast photoluminescence decay dynamics from freestanding strained silicon nanocrystals. Nanoscale Res Lett 2011;6:320.
[22] Shen G, Mao HK. High-pressure studies with X-rays using diamond anvil cells. Rep Prog Phys 2017;80:016101–101654.
[23] Lobanov SS, Prakapenka VB, Prescher C, Konôpkova Z, Liermann H-P, Crispin K, et al. Pressure, stress, and strain distribution in the double-stage diamond anvil cell. J Appl Phys 2015;118:035905.
[24] Fu X-W, Liao Z-M, Liu R, Xu J, Yu D. Size-dependent correlations between strain and phonon frequency in individual ZnO nanowires. ACS Nano 2013;7:8891–8.
[25] Fu X-W, Liao Z-M, Liu R, Lin F, Xu J, Zhu R, et al. Strain loading mode dependent bandgap deformation potential in ZnO micro/nanowires. ACS Nano 2015;9:11960–7.

[26] Gras Ch, Vrel D, Gaffet E, Bernard F. J. Alloys Comput 2001;314:240–50.
[27] Klug H, Alexander LE. X-ray diffraction procedures for polycrystalline and amorphous materials. NY: John Wiley & Sons; 1954.
[28] Hearne GR, Zhao J, Dawe AM, Pischedda V, Maaza M, Nieuwoudt MK, et al. Effect of grain size on structural transitions in anatase TiO_2: a Raman spectroscopy study at high pressure. Phys Rev B 2004;70:134102.
[29] Rehani BR, Joshi PB, Lad KN, Pratap A. Crystallite size estimation of elemental and composite silver nano-powders using XRD, principles. Indian J Pure Appl Phys 2006;44:02.
[30] Thamaphat1 K, Limsuwan P, Ngotawornchai B. Phase Characterization of TiO2 Powder by XRD and TEM. Kasetsart J (Nat Sci) 2008;42:357–61.
[31] Hadjiivanov KI, Klissurski DG. Surface chemistry of titania (anatase) and titania-supported catalysts, Surface chemistry of titania (anatase) and titania-supported catalysts. Chem Soc Rev 1996;25:61–9.
[32] Taziwa R, Meyer EL, Sideras-Haddad E, Erasmus RM, Manikandan E, Mwakikunga BW. Effect of carbon modification on the electrical, structural, and optical properties of TiO_2 electrodes and their performance in labscale dye-sensitized solar cells. Int J Photoenergy 2012;2012.
[33] Sikhwivhilu LM, Mpelane S, Mwakikunga BW, Sinha Ray S. Photoluminescence and hydrogen gas-sensing properties of titanium dioxide nanostructures synthesized by hydrothermal treatments. ACS Appl Mater Interfaces 2012;4:1656–65.
[34] Tian HH, Atzmon M. Comparison of X-ray analysis methods used to determine the grain size and strain in nanocrystalline materials. J Phil Magazine A 1999;79(8).
[35] Weibel A, Bouchet R, Boulc'h F, Knauth P. The big problem of small particles: a comparison of methods for determination of particle size in nanocrystalline anatase powders. Chem Mater 2005;17(9):2378–85.
[36] Fang F, Kennedy J, Manikandan E, Futter J, Markwitz A. Morphology and characterization of TiO2 nanoparticles synthesized by arc discharge. Chem Phys Lett 2012;521:86–90.
[37] Manikandan E, Murugan V, Kavitha G, Babu P, Maaza M. Nanoflower rod wire-like structures of dual metal (Al and Cr) doped ZnO thin films: Structural, optical and electronic properties. Mater Lett 2014;131:225–8.
[38] Manikandan E, Kavitha G, Kennedy J. Epitaxial zinc oxide, graphene oxide composite thin-films by laser technique for micro-Raman and enhanced field emission study. Ceram Int 2014;40(10):16065–70.
[39] Sathyaseelan B, Manikandan E, Sivakumar K, Kennedy J, Maaza M. Enhanced visible photoluminescent and structural properties of ZnO/KIT-6 nanoporous materials for white light emitting diode (w-LED) application. J Alloy Compd 2015;651:479–82.
[40] Mwakikunga BW, Forbes A, Sideras-Haddad E, Scriba M, Manikandan E. Self assembly and properties of C: WO 3 nano-platelets and C: VO 2/V 2 O 5 triangular capsules produced by laser solution photolysis. Nanoscale Res Lett 2010;5(2):389.
[41] Sithole J, Balla Ngom MM, Khamlich D, Manikandan S, Manyala E, Saboungi N, et al. Simonkolleite nano-platelets: Synthesis and temperature effect on hydrogen gas sensing properties. Appl Surf Sci 2012;258(20):7839–43.
[42] Elayaperumal M, Krishnakumar L, Gnanasekaran K, Mani G, Rayappan John Bosco Balaguru, Ladchumananandasivam R, Maaza M. Effective Ammonia Detection Using n-ZnO/p-NiO Heterostructured Nanofibers. IEEE Sens J 2016;16(8):2477–83.
[43] Manikandan E, Moodley MK, Ray SS, Panigrahi BK, Krishnan R, Padhy N. Zinc oxide epitaxial thin film deposited over carbon on various substrate by pulsed laser deposition technique. J Nanosci Nanotechnol 2010;10(9):5602–11.
[44] Sathyaseelan B, Manikandan E, Lakshmanan V, Baskaran I, Sivakumar K. Structural, optical and morphological properties of post-growth calcined TiO2 nanopowder for opto-electronic device application: Ex-situ studies. J Alloy Compd 2016;671:486–92.
[45] Saasa V, Mokwena M, Dhonge B, Manikandan E, Kennedy J, Murmu PP, et al. Optical and structural properties of multi-wall-carbon-nanotube-modified ZnO synthesized at varying substrate temperatures for highly efficient light sensing devices. Sensors Transducers 2015;195(12):9.
[46] Manikandan A, Manikandan E, Meenatchi B, Vadivel S, Jaganathan SK, Ladchumananandasivam R, et al. Rare earth element (REE) lanthanum doped zinc oxide (La: ZnO) nanomaterials: synthesis structural optical and antibacterial studies. J Alloy Compd 2017;723:1155–61.